Fifty-year seasonal variability of East African droughts and floods recorded in Central Afar lake sediments (Ethiopia) and their connections with ENSO

Carlo Mologni [1*], Marie Revel [1], Eric Chaumillon [2], Emmanuel Malet [3], Thibault Coulombier [2], Pierre Sabatier [3], Pierre Brigode [1], Gwenael Hervé [4], Anne-Lise Develle [3], Laure Schenini [1], Medhi Messous [1], Gourguen Davtian [6], Alain Carré, [6], Delphine Bosch [7], Natacha Volto [2], Clément Ménard [5], Lamya Khalidi [6], Fabien Arnaud [3]

[1] Université Côte d'Azur, CNRS, OCA, IRD, Geoazur, 250 rue Albert Einstein, 06500 Valbonne, France.

[2] University of La Rochelle, UMR CNRS 7266 LIENSs, La Rochelle, France.

[3] Environnement Dynamique et Territoire de Montagne (EDYTEM), CNRS, Université Savoie Mont-Blanc, Le Bourget du lac, France.

[4] Laboratoire des Sciences du Climat et de l'Environnement/IPSL, CEA, CNRS, UVSQ, University of Paris-Saclay, Gif-sur-Yvette, France.

[5] EPCC, Centre Européen de Préhistoire, Avenue Léon-Jean Grégory - 66720 – Tautavel, France

[6] Université Côte d'Azur, CNRS, CEPAM – UMR 7264, 24 av. des Diables Bleus 06300 Nice, France.

[7] Géosciences Montpellier, UMR-CNRS 5243, Université de Montpellier, 34095 Montpellier, France

*Corresponding author

Supplementary Materials

A. Seismic survey and imagery of Lake Gemeri

Figure S1 : Satellite image with the location of seismic profiles and the coring sites on Lake Gemeri (Gourguen Davtian, Copernicus Sentinel Data Images©).
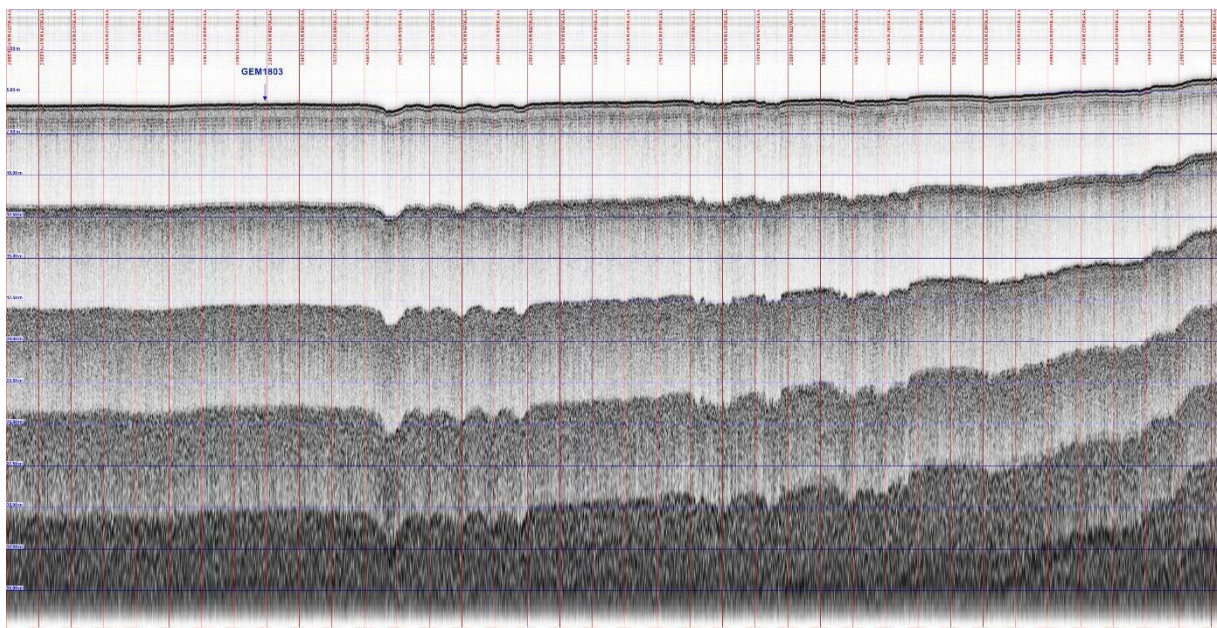
Figure S2 : Seismic profile 006 on Lake Gemeri, with the indication of the coring site (blue arrow; GEM18-03 core).

B. Runoff-rainfall model diagram

$$(1) \quad S_1 = \frac{S + X_1\varphi}{1 + \varphi\dfrac{S}{X_1}} \qquad \text{with} \qquad \varphi = \tanh\left(\frac{P}{X_1}\right)$$

$$(2) \quad P_1 = P + S - S_1$$

$$(3) \quad S_2 = \frac{S_1(1-\psi)}{1 + \psi\left(1 - \dfrac{S_1}{X_1}\right)} \qquad \text{with} \qquad \psi = \tanh\left(\frac{E}{X_1}\right)$$

$$(4) \quad S = \frac{S_2}{\left[1 + \left(\dfrac{S_2}{X_1}\right)^3\right]^{1/3}} \qquad P_2 = S_2 - S$$

$$(5) \quad P_3 = P_1 + P_2$$

$$(6) \quad R_1 = R + P_3$$

$$(7) \quad R_2 = X_5 . R_1$$

$$(8) \quad Q = \frac{R_2^2}{R_2 + 60} \qquad R = R_2 - Q$$
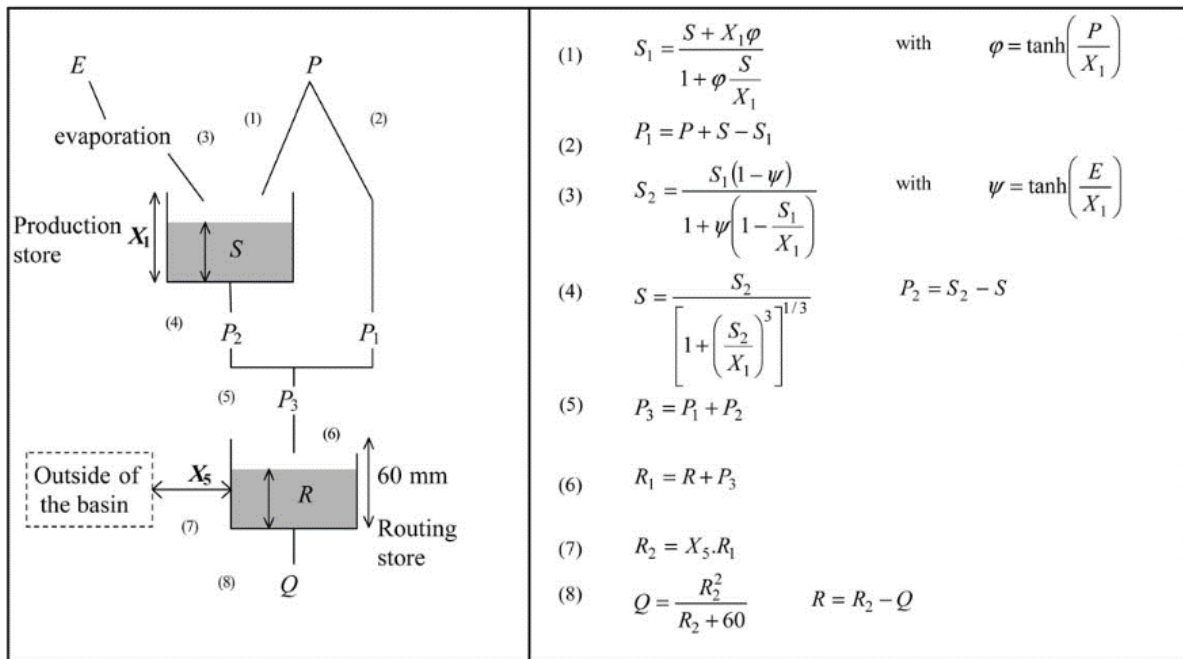
Figure S3 : Diagram of the GR2M model (Mouehli et al., 2006).

C. Principal Components Analysis
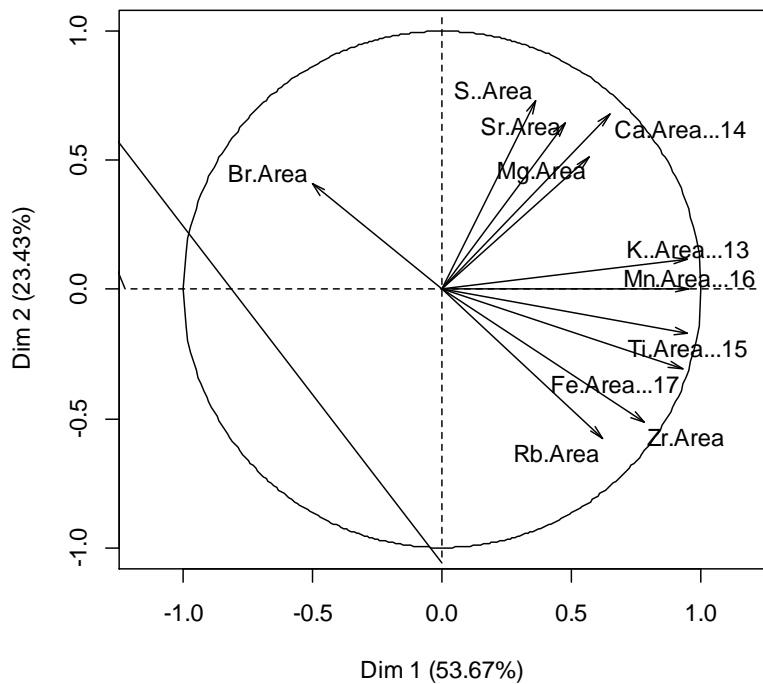
Figure S4 : PCA graph variable of AFA18-02 XRF data analysis on Dim1 with the distinguished End Member-1: Ti, Si, Zr, .

Factor map
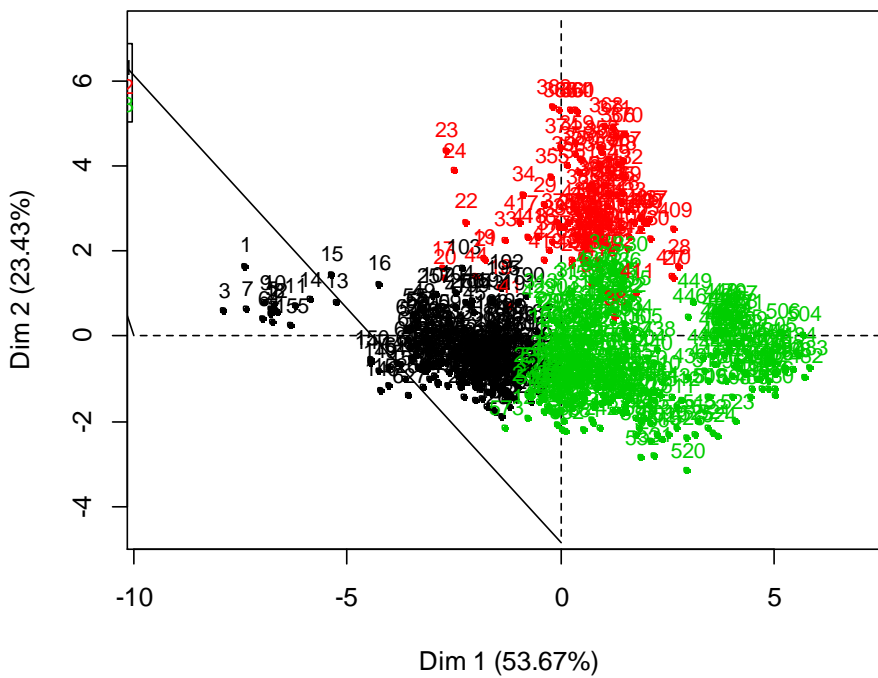
Figure S5 : PCA graph variable of AFA18-02 XRF data analysis on Dim1 with in green the F1 layers, in red the F2/F3 layers.
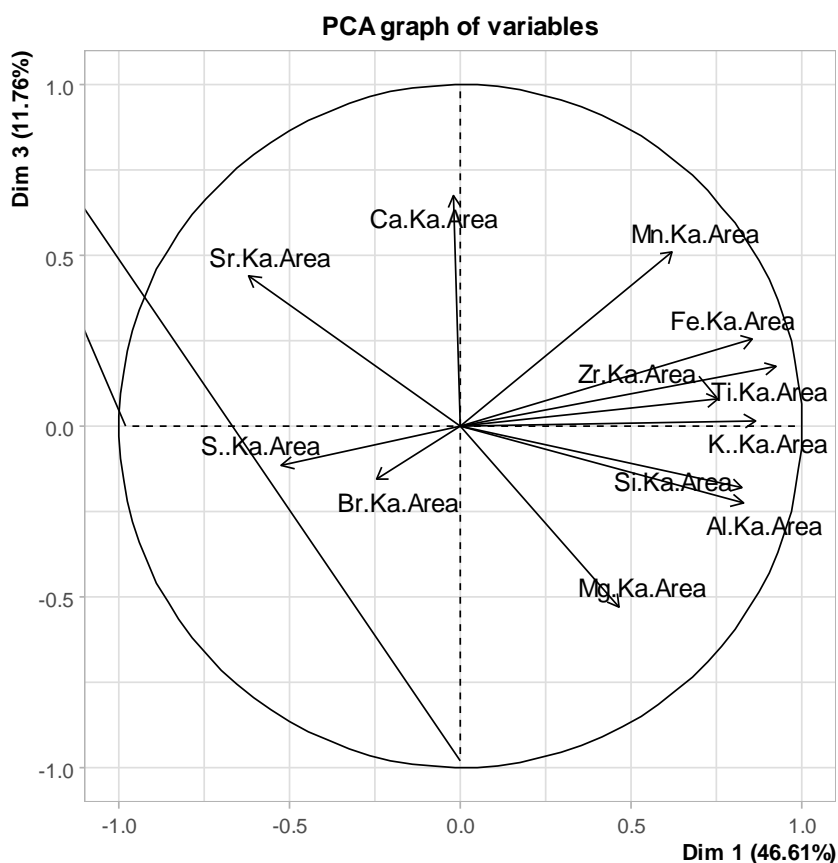
Figure S6: PCA graph variable of GEM18-03/-04B XRF data analysis on Dim1.

D. Paleomagnetic study on Lake Gemeri GEM18-03/04 core

D1. Methods

The two GEM18-03 and GEM18-04B sections were sampled continuously in their centre using u-channels. The u-channel is only partly filled in the first 16 cm of GEM18-03 and between 81 and 89 cm in GEM18-04B (i.e., between 196 and 204 cm of GEM18-03/04B). In GEM18-04B between 14 and 19 cm (i.e., between 129 and 134 cm of GEM18-03/04B), the sediment, stickier at these depths, was also disturbed during subsampling.

All magnetic measurements were performed at the palaeomagnetic laboratory of LSCE (Gif-sur-Yvette, France). The low-field volume magnetic susceptibility (X) was measured every centimeter using a horizontal automated translation system equipped with a MS2-C Bartington coil. In the µ-metal shielded room of LSCE, the natural remanent magnetization (NRM) was measured with a 2 cm step using a helium-free 2G Enterprises cryogenic magnetometer with high-resolution pick-up coils (4.5 cm width on x and y coils, 5.8 cm on z). Stepwise alternating field (AF) demagnetization of the NRM was conducted with the 2G-AF demagnetizer in-line with the magnetometer. The successive steps were fixed to 5, 10, 15, 20, 25, 30, 35, 40, 45 and 50 mT. The direction of the characteristic remanent magnetization (ChRM) was estimated by principal component analysis (Kirschvink, 1980).

In a second step, anhysteretic remanent magnetization (ARM) and isothermal remanent magnetization (IRM) were measured to investigate the ferromagnetic mineralogy. ARM was acquired in a 100 mT AF field and a 50 µT direct current bias field applied along the axis of the u-channel. This ARM was AF demagnetized with the same steps as for the NRM. IRM was acquired in six steps up to 1 T using a 2G

pulsed solenoid in-line with another similar cryogenic magnetometer. After an AF demagnetization of this IRM (always with the same sequence), two additional steps at -1 T and 0.3 T were applied to estimate the contribution of high-coercivity grains to the remanent magnetization with the S-ratio ($S_{0.3\,T}$ = - $IRM_{0.3\,T}$ / $IRM_{-1.0\,T}$).

In order to confirm the rock magnetic identifications, sediment was subsampled in the u-channels at nine different depths (12, 25, 45, 65, 100, 125, 145, 170 and 210 cm). After drying, hysteresis curves up to 1 T, IRM backfield curves and first order reversal curves (FORC) diagrams were performed on ∼ 50 mg chips using a 8600 Lakeshore vibrating sample magnetometer (VSM). Finally, continuous thermomagnetic curves were measured up to 640°C on powders from these nine samples using a Petersen Instruments variable field translation balance (VFTB).

D2. Results

D2.1 Magnetic mineralogy

The profiles of low-field susceptibility (Fig S7a) and NRM intensity (Fig. S7b), as well as those of ARM and IRM intensities, show similar trends. Three different zones can be identified. In the first 20 cm, the low values are probably an effect of the high degree of liquefaction of the sediment. Below, the sediments pedogenized during the drought of the lake in the 1990s are characterized by the highest values of susceptibility and magnetization intensities with a decrease from the top of this layer (around 20-25 cm) to its base around 40 cm. Between 40 and 220 cm, the parameters vary by less than a factor of three, suggesting no large changes of the concentration in magnetic particles through time. This concentration appears relatively high regarding the average values of low-field susceptibility (∼850 × 10^{-6} SI) and NRM intensity (∼70 × 10^{-3} A/m).

All further rock magnetic results, as for example the acquisition and demagnetization curves of ARM and IRM, highlight the homogeneity of the ferromagnetic mineralogy below 40 cm. The S-ratios remain stable between 0.96 and 0.98, which shows the quasi-absence of high coercivity minerals such as hematite or goethite (Fig. S7c). Together with the median destructive field (MDF) values between 18 and 21 mT (Fig. S7d), it suggests that the main magnetic carrier is titanomagnetite not only below 40 cm but also in the 20-40 cm pedogenized sediment. The first 20 cm presents also a high-coercivity phase, but in minor proportion because S-ratio values are always above 0.90. Experiments on discrete samples support these interpretations. Except the sample at 12 cm, all IRM backfield curves are saturated at 300 mT (Fig. S7a). 8/9 thermomagnetic curves are very similar with a single ferromagnetic phase, identified as an almost pure magnetite by its Curie temperature between 560 and 570°C (Fig. S8b). A second phase with a Curie temperature around 100°C, likely a Ti-rich titanomagnetite, is also present in the sample at 170 cm.
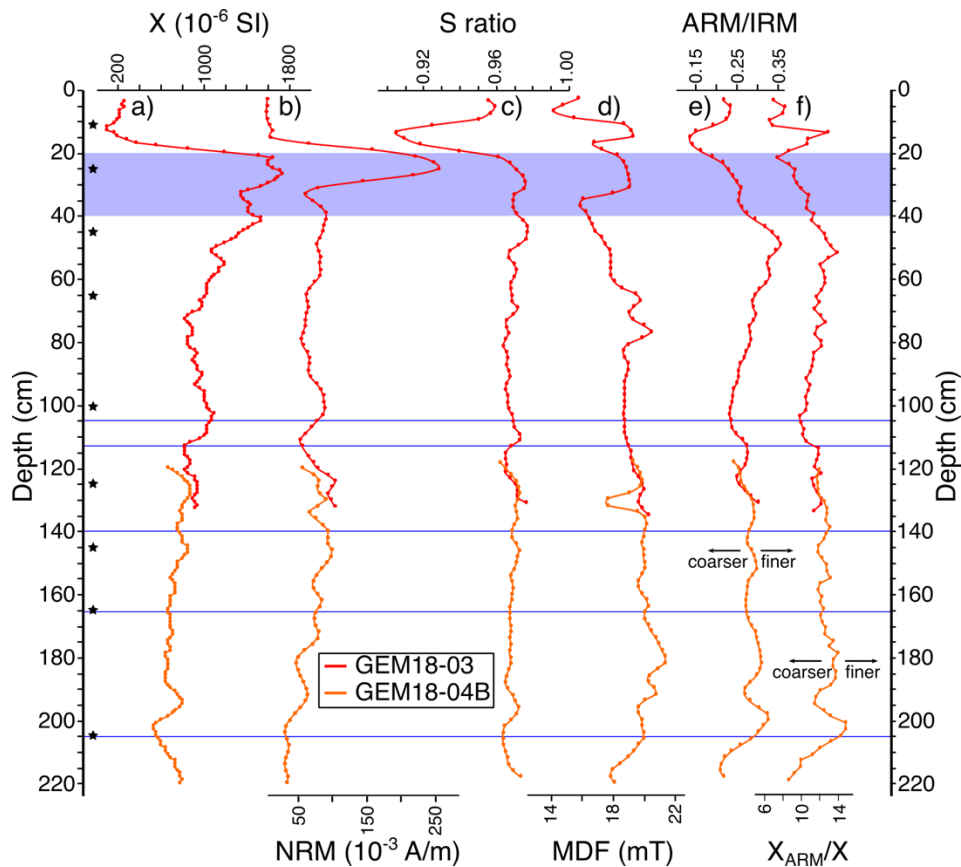
Figure S7: Variation along GEM18-03/04B core of a) low-field magnetic susceptibility (X), b) intensity of the natural remanent magnetization (NRM), c) S-ratio, d) median destructive field (MDF), e) ratio of the intensities of anhysteretic over isothermal remanent magnetization (ARM/IRM) and f) ratio of ARM susceptibility over low-field susceptibility. The two parameters in e-f are proxies of the magnetite grain size). Black stars show depths of discrete samples for rock magnetic experiments. Blue lines indicate depths with abrupt variations in Sr, Fe/Mg and Fe/K ratios, corresponding to pedogenic events.

The ratio of ARM and IRM intensities (ARM/ IRM, Fig. S7e) and the ratio of ARM susceptibility over low-field susceptibility (X_{ARM}/X, Fig. S1f) are proxies of the magnetite grain size. Both parameters do not show a significant variation below 40 cm, especially between 40 and 200 cm. In the Day plot, corresponding discrete samples fit in the pseudo single domain (PSD) field (Fig. S8c), likely indicating a mixture of single-domain (SD) and multidomain (MD) grains. FORCs diagrams are representative of this composition. The pedogenic process results in slightly coarser grains. This behaviour is especially observed in ARM/IRM and X_{ARM}/X curves (Fig. S7e-f) and on the binary plot ARM intensity versus X (Fig. S8), while the Day plot and the FORC diagrams appear less sensitive to this slight size change.
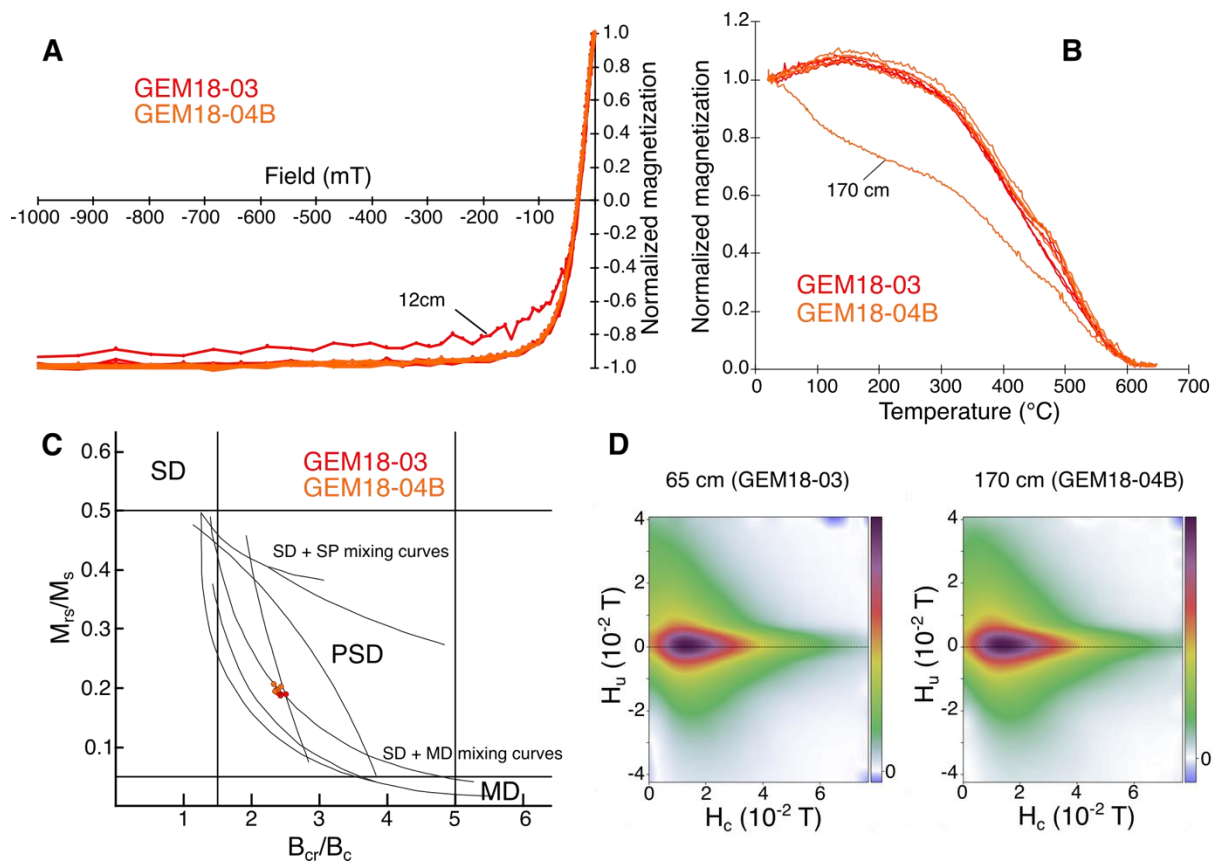
Figure S8: Rock magnetic results on 9 discrete samples from GEM18-03/04 core (at 12, 25, 45, 65, 100, 125, 145, 170 and 210 cm). A) Normalized IRM backfield curves. B) Normalized thermomagnetic curves (only heating curves). C) Day plot of the ratio of the saturation remanent magnetization (M_{rs}) upon the saturation magnetization (M_s) versus the ratio of the coercive remanent field (B_{cr}) upon the coercive field (B_c). D) FORC diagram of two samples.
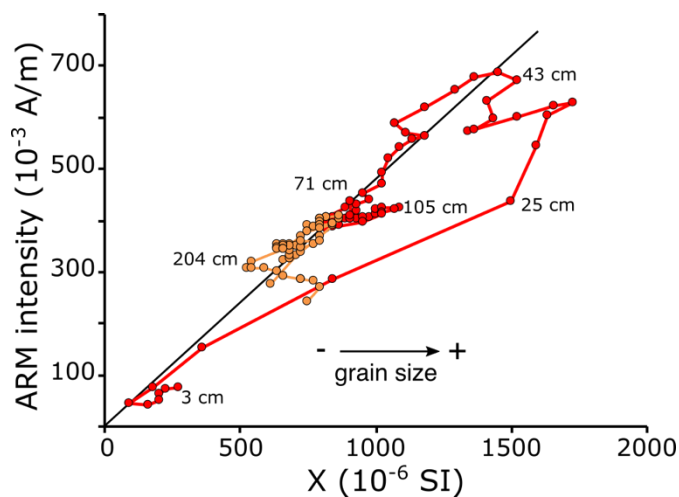
Fig. S9: ARM intensity versus low-field susceptibility plot. Deviations from the line, as between 20 and 40 cm, highlight coarser ferromagnetic grains.

To summarize, all results converge towards a homogeneous ferromagnetic mineralogy composed by almost pure magnetite below 40 cm. These properties, reminding those of volcanic samples, indicate a lithogenic origin of the magnetic grains, which came from the erosion of stratoid basalts and were

transported by the Awash River. These results allow to conclude that the NRM is mainly constituted by a detrital remanent magnetization (DRM) below 40 cm.

The plot of the susceptibility and of the ARM intensity provides information on the variation of the concentration in magnetic grains along the core (Fig. S9). No major changes are observed between 220 and 70 cm with a variation of the two parameters by less than two. From 70 to 40 cm (the lower limit of the pedogenized sediment), the progressive increase may indicate a more important lithogenic input into the lake during the 20th century.

In the case of the pedogenic event recorded between 20 and 40 cm, higher susceptibilities were expected for such soil formation (e.g., Maher and Taylor, 1988). The S-ratios close to 1.0 show that the process is not characterized by the creation of high-coercivity minerals (e.g., hematite or goethite). The average size of magnetite grains is slightly coarser (Fig. S7e-f and Fig. S9). Reminding that the PSD behaviour is explained by a mixture of SD and MD grains, we interpret the increase of the average size by dissolution of the finest SD magnetite grains.

The fact that the magnetic properties of this pedogenesis are not encountered elsewhere in the core highlights that the lake were not affected in its recent past by a drought event as long as in the 1990s. The pedogenic events highlighted by geochemical results at 105, 113, 140, 165.5 and 210 cm are not associated to a significant variation of the magnetic properties, except maybe at 105 and 210 cm (Fig. S7 and S9). The duration of these events is likely too short for the temporal resolution of the magnetometer. We therefore consider that the core GEM18-03/04B is not significantly affected by pedogenesis below 40 cm, allowing to investigate the secular variation of the geomagnetic field.

D2.2 Directional study

After removing a minor component of magnetization, probably of viscous origin, all Zijderveld diagrams highlight a stable ChRM above 10 mT (15-20 mT for a few samples) (Fig. S10). This ChRM is well-defined with an average maximum angular deviation (MAD) value of 1.5° (Fig. D5a).
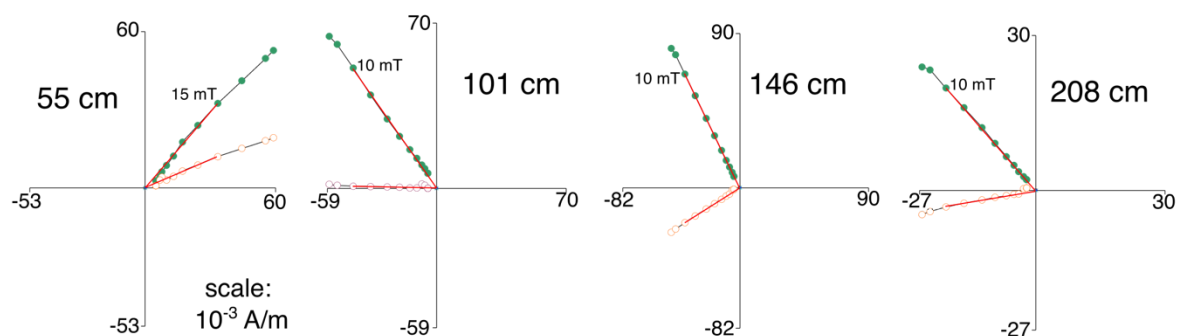
Figure S10: AF demagnetization results with examples of Zijderveld plots. The open and full circles are the projections upon vertical and horizontal planes respectively. The red line shows the direction of the ChRM component.

The variation of declination and inclination through the u-channels are plotted in Figure S5b-c. The fast variation in the first 20 cm reflects the difficulty to preserve the signal in liquefied sediment during coring. For interpretation, we also discarded the 20-40 cm depths at which the initial remanent magnetization was likely modified by pedogenic processes during drying-up of the lake from 1984 to 1999. In GEM18-04B, the slight directional variations between 129 and 134 cm and between 196-204 cm can be explained by problems during preparation of the u-channel and the directions around these depths were considered unreliable.

The core was not azimuthally oriented and the declination requires adjustment. For GEM18-03 section, we based on the age model established with short-lived radionuclides (^{210}Pb and ^{137}Cs) and on the prediction at Lake Gemeri of the International Geomagnetic Reference Field model IGRF-13 (Alken et al., 2021). In 1978 CE, i.e. at 42 cm depth, the expected declination is 6°. To obtain this value, all declination values of GEM18-03 were shifted by +35°. The section GEM18-04B overlaps GEM18-03 between 118 and 126 cm. The comparison of average declination in this range results in a shift by +100° of GEM18-04B. The consistency of declination record between the two sections is satisfactory (Fig. D5d). In inclination, the two sections slightly differ at 188-126 cm (Fig. S11c). This difference probably comes from the fact that coring was not exactly vertical. At 42 cm depth, the measured inclination is 6° lower than the value predicted by IGRF-13 model. Adjusting GEM18-03 by this value makes its inclination record consistent with the one of GEM18-04B (Fig. S11e).

The inclination and declination GEM18-03/04B record shows short oscillations that are probably not related to secular variation of the geomagnetic field but rather to small disturbances of the sediment during or slightly after deposition (e.g., with bioturbations). To minimize the effect of these short oscillations and make easier the chronological interpretation, the signal was smoothed with a 8-cm sliding window.
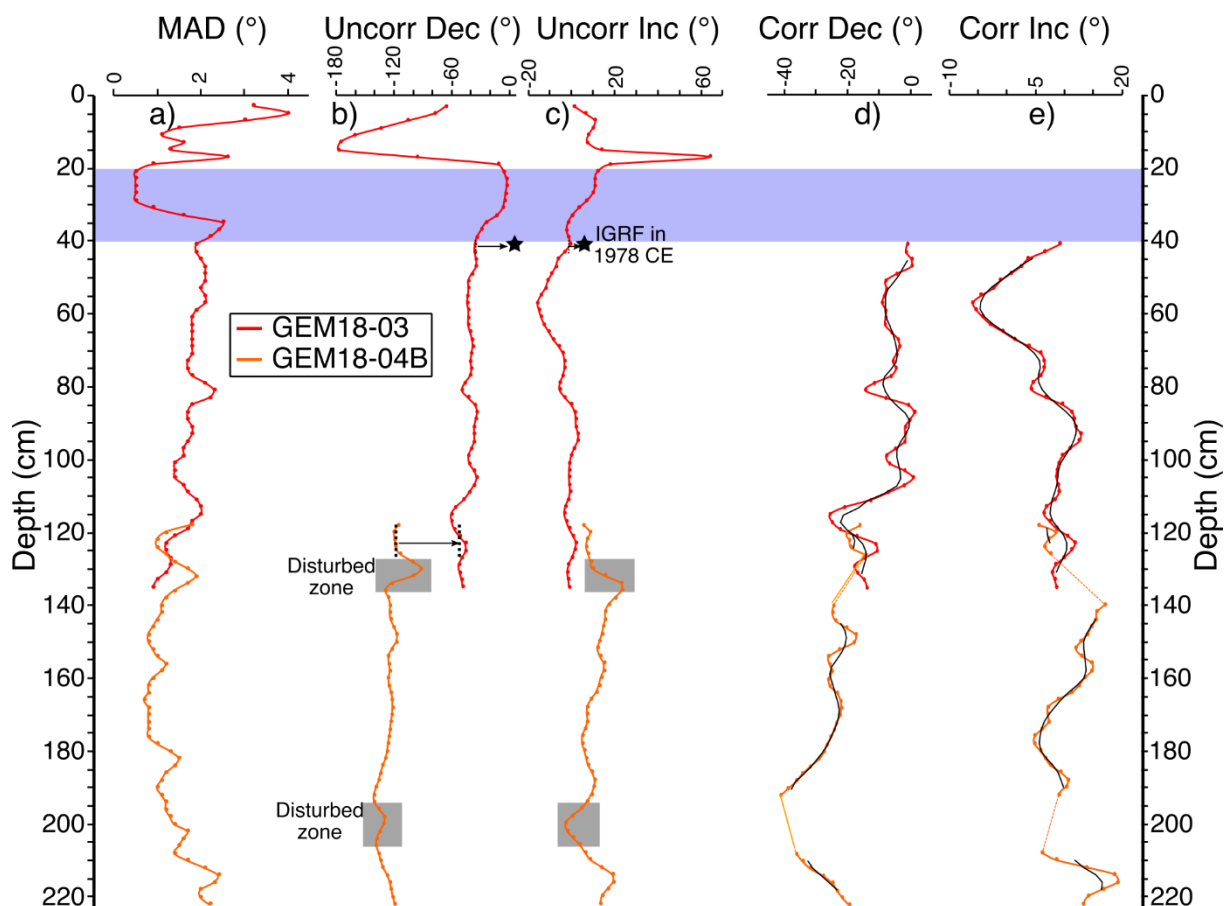
Figure S11: Direction of the Characteristic Remanent Magnetization (ChRM). (a) Maximum angular deviation (MAD) quantifying the quality of the direction. (b) Declination and (c) inclination raw values without orienting correction. Grey shaded areas correspond to discarded data because of disturbances in the sediment during the sampling process. (d) Declination and e) inclination after orientation with IGRF values in 1980 at 42 cm for the top and adjustment between the two sections using 118-125 cm average values. The thin black curves show the variation after smoothing with a 8-cm sliding window. Blue area highlight sediment affected by pedogenesis during the drought of the Lake in the 90s.

D2.3 Determination of the relative palaeointensity (RPI)

Below 40 cm, magnetic properties appear very favourable to the study of the RPI, because the ChRM is stable and because ferromagnetic grains are homogeneous in nature and size with a lithogenic origin and a low variation of their concentration along the core. The RPI estimation consists in a normalization of the NRM intensity by ARM intensity, IRM intensity or low-field susceptibility. ARM is generally preferred because it activates the same ferromagnetic grains as the NRM. We tested the three normalization factors using the NRM, IRM and ARM intensities remaining after 15 mT AF step, in order to remove the effect of the viscous component. The RPI was not estimated between 129 and 134 cm and between 196-204 cm for the same reasons as for the direction.

The three normalization factors provide similar RPI results, highlighting their robustness (Fig. S12). They show a relatively stable variation up to ~110 cm before an increase followed by a plateau from ~130 to 170-175 cm. A decrease of the RPI is finally observed up to 220 cm. The precise rate of this decrease is poorly constrained because of the lack of reliable data between 196 and 204 cm.
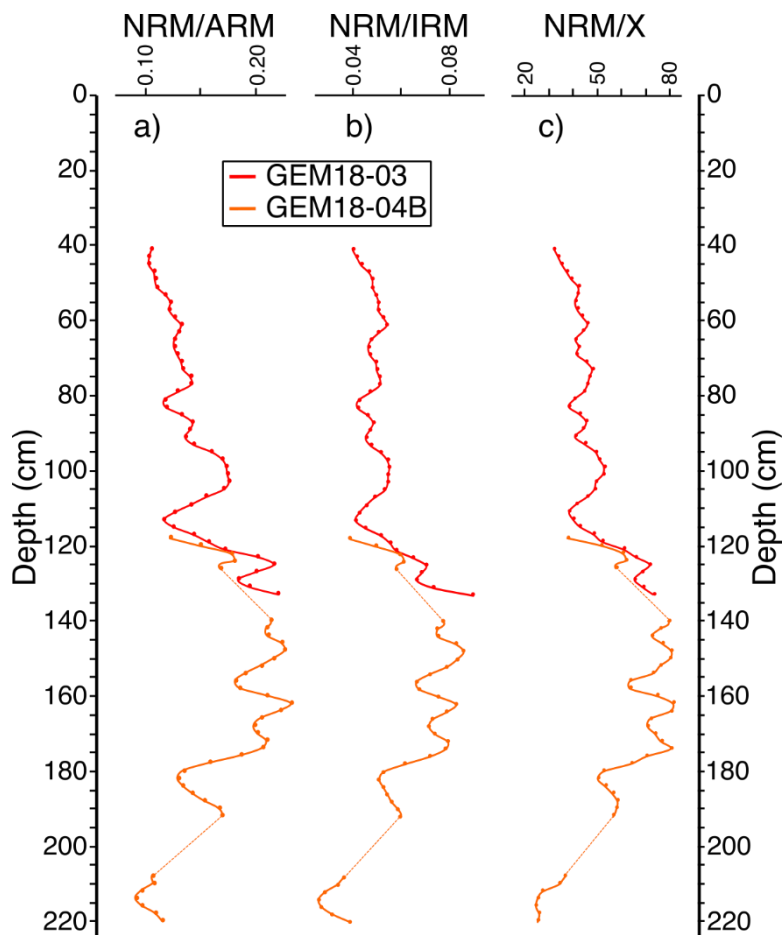
Figure S12: Relative palaeointensity records obtained on GEM18-03/04B using a) ARM intensity, b) IRM intensity and c) low-field susceptibility as normalizer of the NRM intensity. The first one was chosen for the comparison with geomagnetic models.

References

Alken, P., Thébault, E., Beggan, C.D. et al., 2021. International Geomagnetic Reference Field : the thirteenth generation. Earth Planets Space 73, 49. https://doi.org/10.1186/s40623-020-01288-x

Kirschvink, J.L., 1980. The least squares lines and plane analysis of palaeomagnetic data. Geophys. J. R. Astron. Soc. 62, 699–718.

Maher, B., Taylor, R., 1988. Formation of ultrafine-grained magnetite in soils. Nature, 336, 368-370.

E. Loss on Ignition

Sample Name	Weigh 12h 65°	Weigh 24h 105°	Weight 5h 550°	Residual H2O	LOI (%)	Total depth
GEM18-03_9	4,313	3,9168	3,5865	9,18618131	8,43290441	9
GEM18-03_30	6,385	5,8862	5,3821	7,81205951	8,56409908	30
GEM18-03_103	4,552	4,1855	3,8146	8,05140598	8,86154581	103
GEM18-04B_80-81	2,806	2,5323	2,3329	9,75409836	7,8742645	194
GEM18-04B_104	4,693	4,2898	3,901	8,59151928	9,0633596	218

Tab. S13: Loss on Ignition table results on GEM18-03/-04 core

F. Clay X-Ray Diffraction
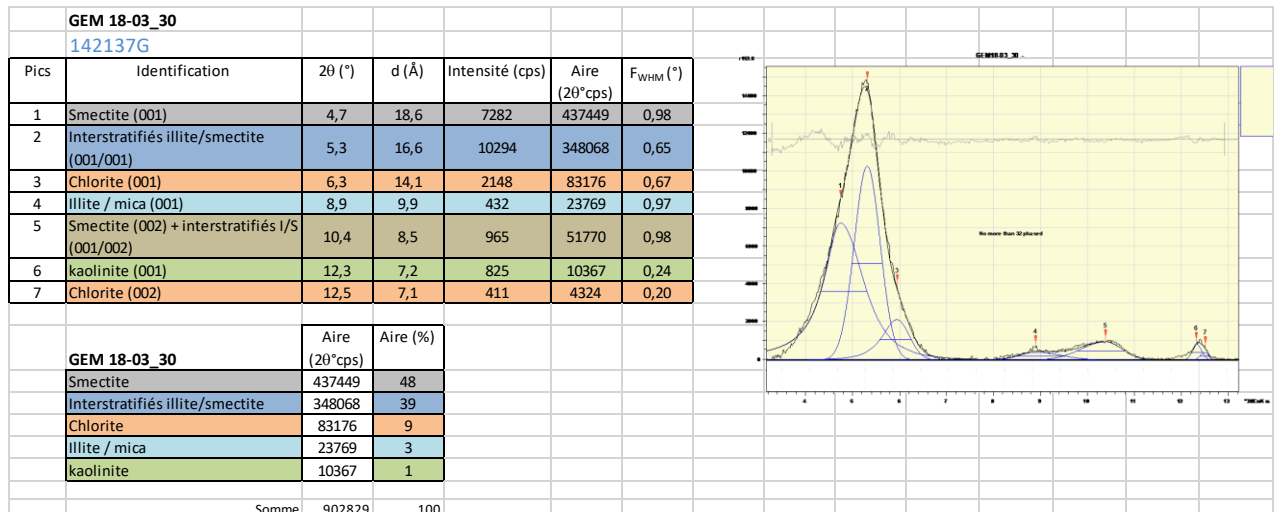
Figure S14 : Clay XRD diffraction results of GEM18-03 30 cm sample
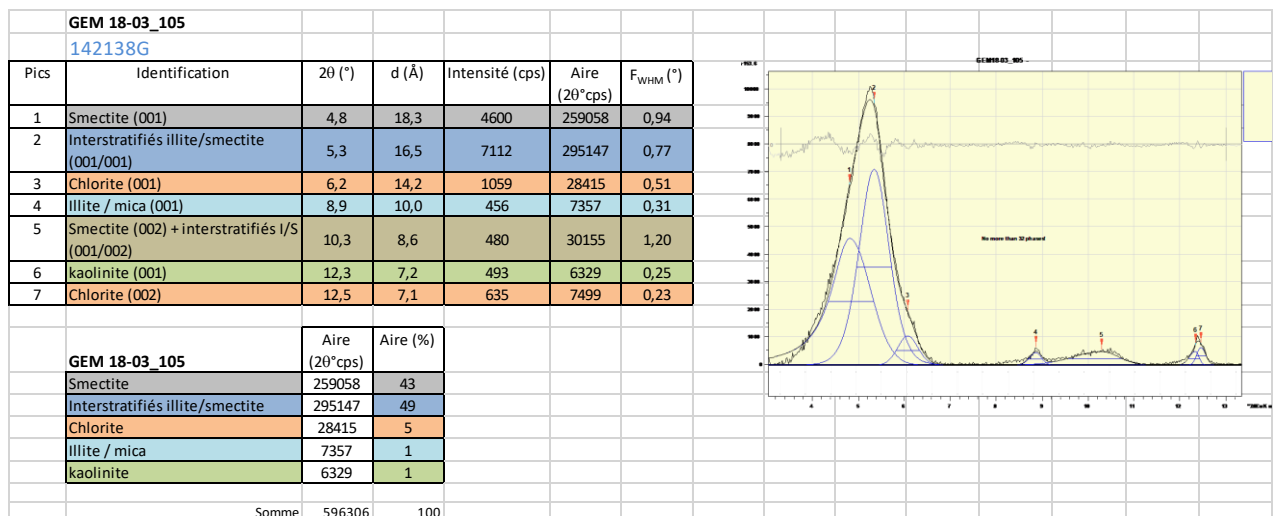
Figure S15 : Clay XRD diffraction results of GEM18-03 105 cm sample

	GEM 18-04B_10					
	142139G					
Pics	Identification	2θ (°)	d (Å)	Intensité (cps)	Aire (2θ°cps)	F_WHM (°)
1	Smectite (001)	4,6	19,2	2726	116545	0,80
2	Interstratifiés illite/smectite (001/001)	5,3	16,8	11515	548973	0,81
3	Chlorite (001)	6,2	14,2	932	31909	0,51
4	Illite / mica (001)	8,9	10,0	478	6734	0,27
5	Smectite (002) + interstratifiés I/S (001/002)	10,3	8,6	586	40121	1,12
6	kaolinite (001)	12,4	7,2	798	8717	0,21
7	Chlorite (002)	12,5	7,1	567	5651	0,19

GEM 18-04B_10	Aire (2θ°cps)	Aire (%)
Smectite	116545	16
Interstratifiés illite/smectite	548973	77
Chlorite	31909	4
Illite / mica	6734	1
kaolinite	8717	1
Somme	712878	100

Figure S16 : Clay XRD diffraction results of GEM18-04 10 cm sample

	GEM 18-04B_80					
	142140G					
Pics	Identification	2θ (°)	d (Å)	Intensité (cps)	Aire (2θ°cps)	F_WHM (°)
1	Smectite (001)	4,7	18,6	5369	326944	0,98
2	Interstratifiés illite/smectite (001/001)	5,3	16,6	9391	430048	0,83
3	Chlorite (001)	6,2	14,2	1194	36229	0,58
4	Illite / mica (001)	8,8	10,0	490	10824	0,42
5	Smectite (002) + interstratifiés I/S (001/002)	10,2	8,6	762	50274	1,05
6	kaolinite (001)	12,3	7,2	717	9888	0,26
7	Chlorite (002)	12,5	7,1	585	7333	0,24

GEM 18-04B_80	Aire (2θ°cps)	Aire (%)
Smectite	326944	40
Interstratifiés illite/smectite	430048	53
Chlorite	36229	4
Illite / mica	10824	1
kaolinite	9888	1
Somme	813933	100

Figure S17: Clay XRD diffraction results of GEM18-04 80 cm sample

	GEM 18-04B_105					
	142141G					
Pics	Identification	2θ (°)	d (Å)	Intensité (cps)	Aire (2θ°cps)	F_WHM (°)
1	Smectite (001)	4,7	18,8	4778	254956	0,87
2	Interstratifiés illite/smectite (001/001)	5,3	16,7	9346	362609	0,67
3	Chlorite (001)	6,2	14,1	1977	93505	0,78
4	Illite / mica (001)	8,8	10,0	391	19356	0,94
5	Smectite (002) + interstratifiés I/S (001/002)	10,2	8,6	678	38446	1,09
6	kaolinite (001)	12,3	7,2	754	8653	0,22
7	Chlorite (002)	12,5	7,1	533	5971	0,21

GEM 18-04B_105	Aire (2θ°cps)	Aire (%)
Smectite	254956	34
Interstratifiés illite/smectite	362609	49
Chlorite	93505	13
Illite / mica	19356	3
kaolinite	8653	1
Somme	739079	100

Figure S18: Clay XRD diffraction results of GEM18-04 105 cm sample

G. GEM18 ICP-MS and XRF geochemistry results

	GEM18-03_25	GEM18-03_60	GEM18-03_90	GEM18-03_100	GEM18-04B_60
Major Elements (wt%)					
Na_2O	1,14	0,93	0,83	0,89	0,68
MgO	4,29	3,74	3,53	3,40	3,55
Al_2O_3	13,44	14,44	13,46	13,13	15,37
K_2O	1,61	1,30	1,23	1,29	1,52
CaO	9,93	8,68	10,22	11,16	5,82
TiO_2	1,32	1,24	1,20	1,28	1,31
MnO	0,17	0,15	0,17	0,20	0,16
P_2O_5	0,30	0,30	0,29	0,31	0,30
SiO_2	43,25	45,67	43,77	43,22	48,61
Fe_2O_3 (T)	9,40	9,52	9,21	9,33	10,30
LOI	16,00	14,43	17,54	16,33	12,10
Tot.	100,84	100,41	101,45	100,53	99,72

Trace Elements (ppm)	GEM18-03_25	GEM18-03_60	GEM18-03_90	GEM18-03_100	GEM18-04B_60
Li	14,11	15,25	14,34	13,81	16,75
V	157,64	174,46	159,05	162,99	158,59
Cr	81,56	84,94	78,43	76,58	83,58
Ni	70,12	71,47	63,87	64,03	68,82
Cu	60,67	63,79	61,98	64,85	63,04
Zn	105,29	111,09	106,46	103,70	124,84
Rb	44,45	47,67	44,89	43,19	57,27
Sr	469,9	367,2	379,0	399,4	218,3
Y	41,42	41,78	39,78	40,76	49,18
Zr	252,17	259,69	247,55	260,73	346,42
Nb	79,10	77,73	77,05	90,88	97,17
Cd	0,38	0,39	0,36	0,36	0,41
Sn	2,30	2,30	2,31	2,40	2,66
Sb	0,20	0,23	0,21	0,23	0,23
Cs	1,69	1,80	1,69	1,59	2,06
Ba	321,7	317,8	284,3	285,8	276,4
La	38,60	38,76	36,45	36,87	46,09
Ce	90,90	89,70	84,47	85,21	104,20
Pr	10,51	10,42	9,78	9,79	12,06
Nd	43,96	43,08	40,46	40,63	49,16
Sm	9,10	8,97	8,35	8,49	10,06
Eu	2,20	2,16	1,96	2,03	2,27

Gd	8,51	8,42	7,86	7,88	9,32
Tb	1,32	1,30	1,23	1,24	1,46
Dy	7,79	7,83	7,33	7,45	8,87
Ho	1,55	1,54	1,48	1,48	1,78
Er	4,29	4,20	4,01	4,11	4,99
Tm	0,60	0,59	0,57	0,58	0,71
Yb	3,83	3,86	3,72	3,74	4,61
Lu	0,57	0,56	0,56	0,55	0,68
Hf	7,04	7,02	6,63	6,80	8,99
Ta	5,05	4,77	4,94	5,60	5,99
Pb	3,85	3,85	3,58	3,79	4,59
Th	6,73	6,93	6,50	6,42	8,59
U	1,50	1,79	1,39	1,34	1,61

Table S1

Major Elements	Total depth (cm)	Sr (ppm)	Zr (ppm)	Si/Al	Fe/Mg	Sr/Th	U/Th
GEM18-03_25	25	469,879575	252,165771	3,21895008	2,19068551	69,8434241	0,2225589
GEM18-03_60	60	367,234604	259,687387	3,16273427	2,54947578	53,0194095	0,25798047
GEM18-03_90	90	379,000712	247,554917	3,25242937	2,60581545	58,2721824	0,21361314
GEM18-03_100	100	399,36124	260,734981	3,29184592	2,74671545	62,243145	0,20830875
GEM18-04B_60	174	218,341397	346,423498	3,16223101	2,90148572	25,4038698	0,18775804
AFA18-02A-12	12	423,4	271,65	3,48591013	2,07142857	63,76	0,25
AFA18-02B-110	110	568,2	216,32	3,72121711	1,9638009	94,7	0,25

Table S2
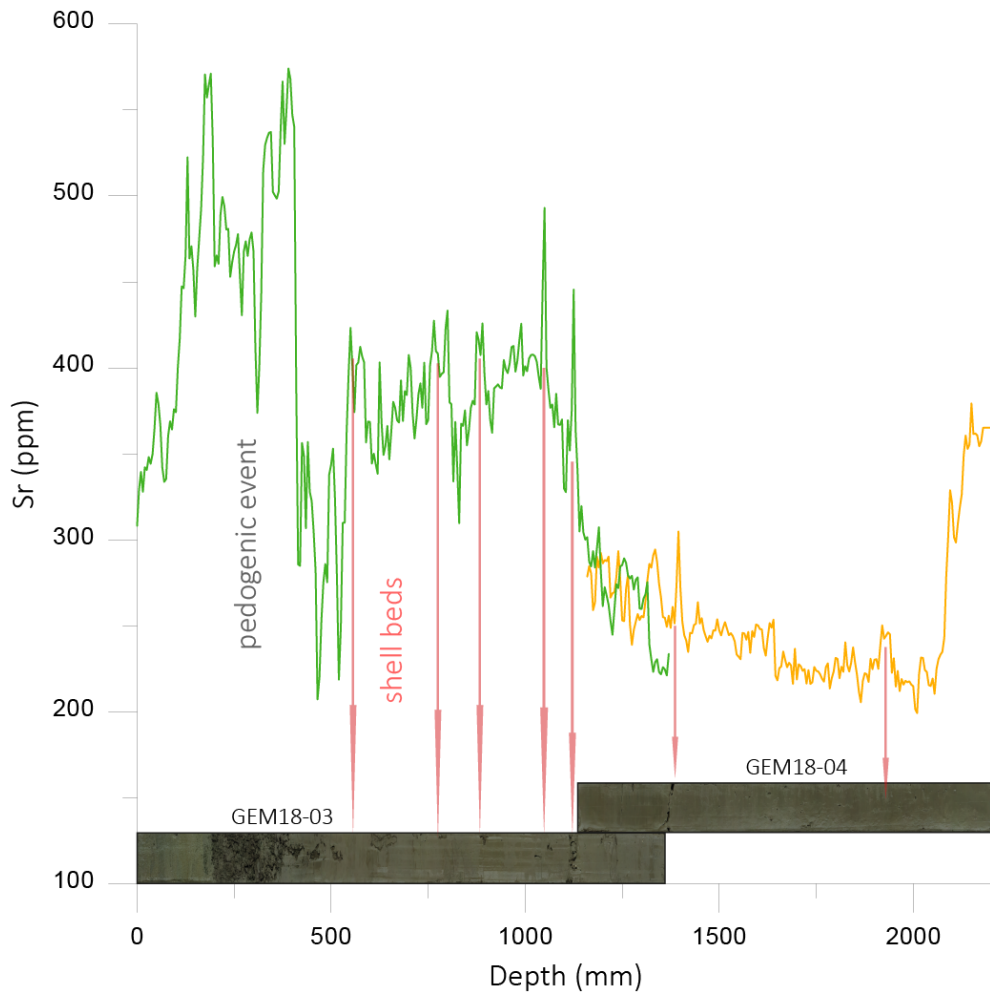
Figure S19: Sr values of GEM18-03 core with indicated the shell beds layers.
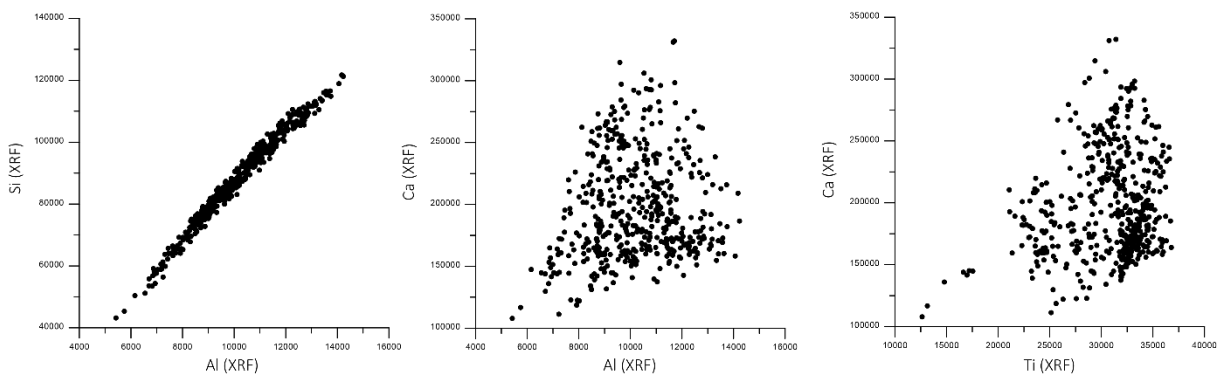
Figure S20 : Plots of Major elements (Al/SI, Al/Ca, Ti/Ca) measured by XRF-core scanner.

H. Radiocarbon material sampling AFA18-02 core
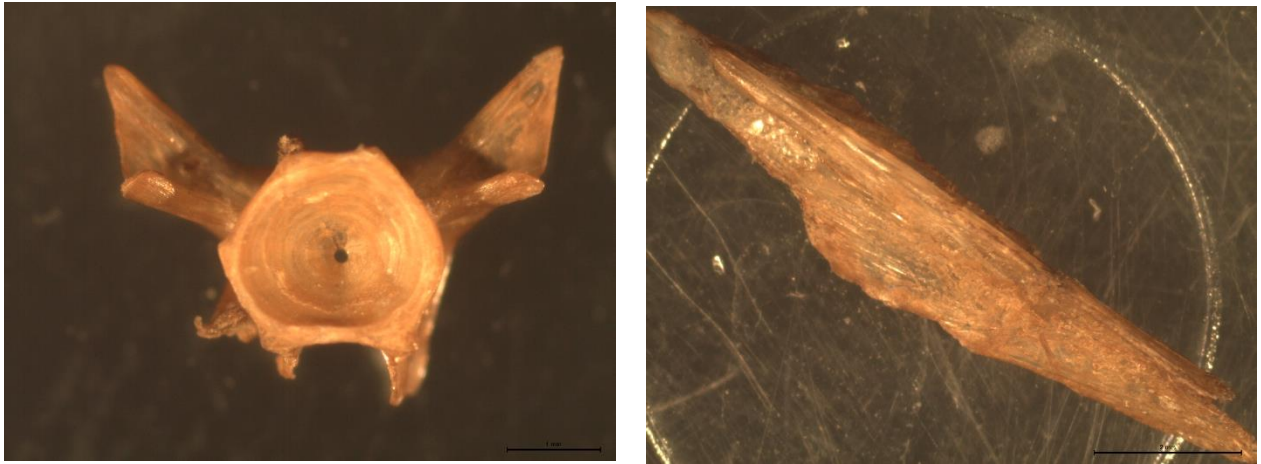
Figure S21 : Haplotilapiini cf. Oreochromis niloticus from 61 and 149.5 cm depth of the AFA18-02 core. GifA20055/ECHo3328 and GifA20056/ECHo3327 samples respectiveli (see Tab 2 in the main text of the article).

N°	Sample Name	Total Depth (cm)	Material	Weight	to the Lab	Lab Code	Dated	mg C	Delta C13	median	σ	cal. BP/AD
1	AFA18-02A_10.5-11	10.5-11	bulk organic sediment	4 g	Artemis	SacA57084	dated	0,60	-28,10	387	47	BP
2	AFA18-02A_44	44	bulk organic sediment	4 g	Artemis	SacA57085	dated	0,90	-19,70	598	35	BP
3	AFA18_02A_61	61	Fish bone	9.2 mg	LSCE MICHADAS	GifA20055/ECHo3328	dated			2008 AD		AD
4	AFA18-02A_61	61	bulk organic sediment	4 g	Artemis	SacA59130	dated	1,19	-24,5	603	31	BP
5	AFA18-02A_76	76	bulk organic sediment	4 g	Artemis	SacA57086	dated	1,03	-20,60	429	57	BP
6	AFA18-02B_8-8.5	92	bulk organic sediment	4 g	Artemis	SacA57087	dated	1,09	-21,90	177	86	BP
7	AFA18-02B_35-39	118-122	vegetal macroremains	1.2 mg	LSCE MICHADAS	GifA20052/ECHo3259	dated			2000		AD
8	AFA18-02B_50.5-51	134.5-135	bulk organic sediment	3 g	Artemis	SacA57088	dated	1,21	-23,40	post 1950		AD
9	AFA18-02B_51-53	134-136	vegetal macroremains	1.2 mg	LSCE MICHADAS	GifA20053/ECHo3260	dated			1992		AD
12	AFA18_02B_66.5	149,5	Fish bone	18.8 mg	LSCE MICHADAS	GifA20056/ECHo3327	dated			1985		AD
13	AFA18-02B_67	150	bulk organic sediment	5 g	Artemis	SacA59131	dated	1,08	-21,1	388	46	BP
14	AFA18-02B_82.5-83.5	165.5-166.5	vegetal macroremains		LSCE MICHADAS	GifA20054/ECHo3261	dated			1982		AD
15	AFA18-02B_81.5-82	165.5-170	bulk organic sediment	4 g	Artemis	SacA57089	dated	1,14	-22,10			

Core AFA18-02 _ Samples for 14C Dating

Bulk OM

Fish bone

Vegetal macrorests

Figure S22 : List of radiocarbon samples detailed information from AFA18-02 sequence..

I. Radiocarbon material sampling GEM18-03/-04B core

	Core GEM18-03/04B _ Samples for 14C Dating							
	Sampling							
N°	Sample Name	Total Depth (cm)	Material	Weight	Lab	Lab Code	mg C	Delta C13	Conventional age
1	GEM18-03_14-15	14	organic sediment	4.3	Artemis	SacA57090	1,06	-20,70	175 ± 30
2	GEM18-03_48-49	48,5	organic sediment	4.77	Artemis	SacA57091	0,90	-14,00	170 ± 30
3	GEM18-03_48-49_malaco	48,5	shell (melania)		Artemis	SacA57092	1,44	-2,4	post 1950
4	GEM18-03_84	84	organic sediment	~4 g	Artemis	SacA59132	1,02	-19,7	1975 ± 30
5	GEM18-03_84_malaco	84	shell (melania)	~4 g	Artemis	SacA59133	1,21	-0,1	725 ± 30
6	GEM18-03_113	113	organic sediment	4.165	Artemis	SacA57093	1,12	-23,10	1760 ± 30
7	GEM18-03_120	120	organic sediment	~4 g	Artemis	SacA59134	1,8	-18,2	2465 ± 30
8	GEM18-04B_10	124	organic sediment	~4 g	Artemis	SacA59135	1,03	-17,1	2465 ± 30
9	GEM18-04B_53	167	organic sediment	4.3 g	Artemis	SacA59136	1,02	-17,8	2845 ± 30
10	GEM18-04B_53_malaco	167	shell (melania)	4.77 g	Artemis	SacA59137	1,38	-5,5	680 ± 30
11	GEM18-04B_100	214	organic sediment	4.9	Artemis	SacA57094	1,01	-23,30	2330 ± 30
12	GEM18-04B_106	220	organic sediment	4g	Artemis	SacA59138	1	-19,3	1785 ± 30

Figure S23 : List of radiocarbon samples detailed information from GEM18-03/-04B sequence.

J. Grain Size distribution
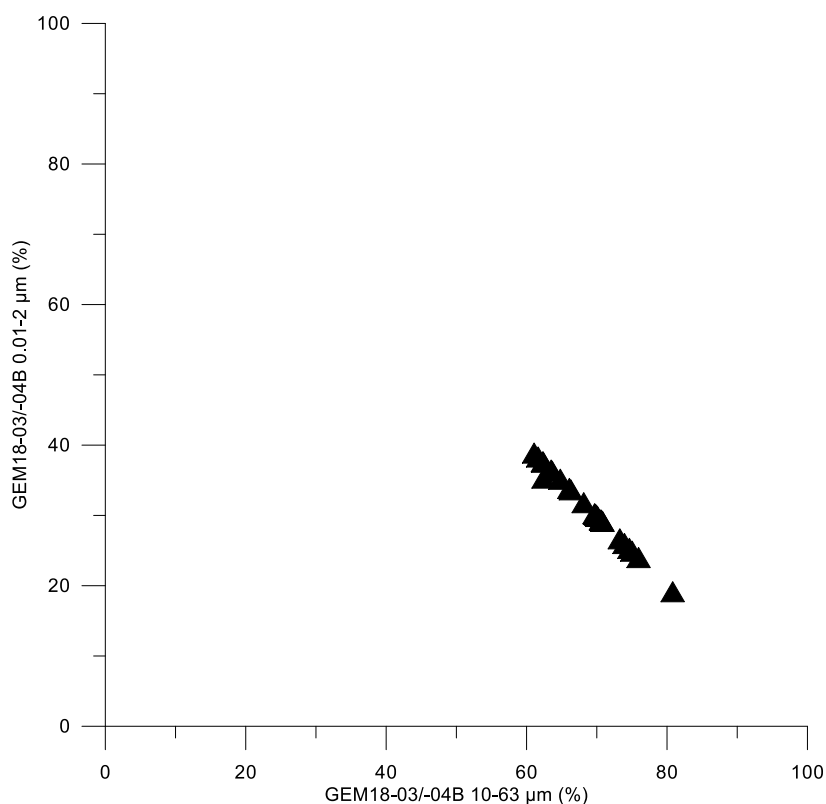
Figure S24 : Plot of GEM18-03/-04B core 0.01-2µm vs 10-63µm grain size
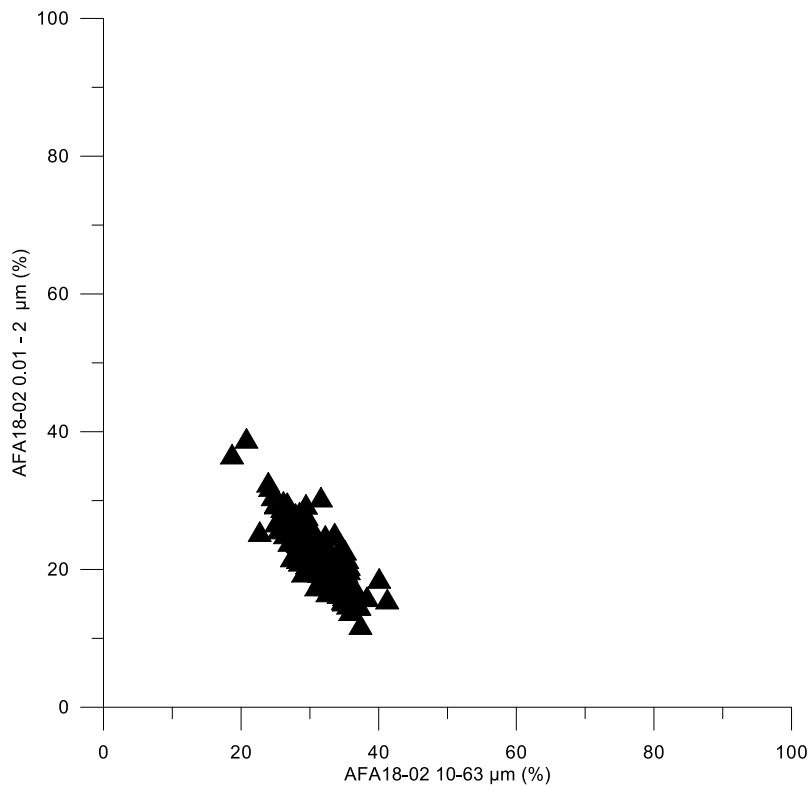
Figure S25 : Plot of AFA18-02-A core 0.01-2µm vs 10-63µm grain size

E. Stokes Law calculation of Lake Afambo sediments

Formula parameter	Description	Value	Unit
g	Gravity acceleration	9.80665	m/s^2
µ	Medium viscosity of water at 28°C	0.0008324	Pa.s
p_m	Medium density of water at 28°C (calculated from conductivity and temperature measurements in the Lake Afambo obtained in October 2023; conductivity = 2916 uS)	0.9956	kg/m^3
p_p	Particle density (smectite)	2.2	g/cm^3
d	Medium particle diameter (total grain size mean of AFA18-02 core)	0.006748	mm
v	**Terminal Velocity**	**0.0000655379**	**m/s**

Table S3 : Lake Afambo parameters for the Stokes Law calculation.

$$v = g \times d^2 \times (\rho p - \rho m)/(18 \times \mu)$$

The Stokes Law calculation (McCave, 2005) for Lake Afambo sediments indicates a 0.0000655379 m/s of sedimentation speed. For the 17m of water depth of the lake Afambo, a sediment particle takes an average of ~72 hr to reach the bottom of the lake.

McCave, I.N., 2005. SEDIMENTARY PROCESSES | Deposition from Suspension, in: Selley, R.C., Cocks, L.R.M., Plimer, I.R. (Eds.), Encyclopedia of Geology. Elsevier, Oxford, pp. 8–17. https://doi.org/10.1016/B0-12-369396-9/00490-1